

Automated Flaw Detection in Aluminum Castings Based on the Tracking of Potential Defects in a Radioscopic Image Sequence

Domingo Mery, *Member, IEEE*, and Dieter Filbert

Abstract—This paper presents a new method for inspecting aluminum castings automatically from a sequence of radioscopic images taken at different positions of the casting. The classic image-processing methods for flaw detection of aluminum castings use a bank of filters to generate an error-free reference image. This reference image is compared with the real radioscopic image, and flaws are detected at the pixels where the difference between them is considerable. However, the configuration of each filter depends strongly on the size and shape of the structure of the casting under inspection. A new two-step technique is proposed to detect flaws automatically and that uses a single filter. First, the method identifies potential defects in each image of the sequence, and second, it matches and tracks them from image to image. The key idea of this paper is to consider as false alarms those potential defects which cannot be tracked in the sequence. The robustness and reliability of the method have been verified on both real data in which synthetic flaws have been added and real radioscopic image sequences recorded from cast aluminum wheels with known defects. Using this method, the real defects can be detected with high certainty. This approach achieves good discrimination from false alarms.

Index Terms—Aluminum castings, automated inspection, computer vision, flaw detection, image segmentation, X-ray testing.

I. INTRODUCTION

RADIOSCOPY is increasingly being used as a tool for non-destructive testing in industrial production. An example is the serial examination of cast light-alloy workpieces used in the car industry, like aluminum wheels and steering gears [1]. The material defects occurring in the casting process such as cavities, gas, inclusions, and sponging must be detected to satisfy the safety requirements; consequently, it is necessary to check 100% of the parts. Since most defects are not visible, X-ray imaging is used for this task. An example of a radioscopic image is shown in Figs. 1 and 2.

Manuscript received December 5, 2000; revised February 21, 2002. This paper was recommended for publication by Associate Editor P. Allen and Editor S. Hutchinson upon evaluation of the reviewers' comments. This work was supported in part by the German Academic Exchange Service (DAAD), in part by the Technical University of Berlin, in part by YXLON International X-Ray GmbH, Hamburg, and in part by the Universidad de Santiago de Chile, Santiago, Chile. This paper was presented in part at the 15th World Conference on Non-Destructive Testing, Rome, Italy, October 15–21, 2000.

D. Mery is with the Universidad de Santiago de Chile, Departamento de Ingeniería Informática, Santiago, Chile (e-mail: dmery@iee.org).

D. Filbert is with the Technische Universität Berlin, Fakultät IV Elektrotechnik und Informatik, Institut für Energie- und Automatisierungstechnik, D-10587 Berlin, Germany (e-mail: dieter.filbert@tu-berlin.de).

Digital Object Identifier 10.1109/TRA.2002.805646

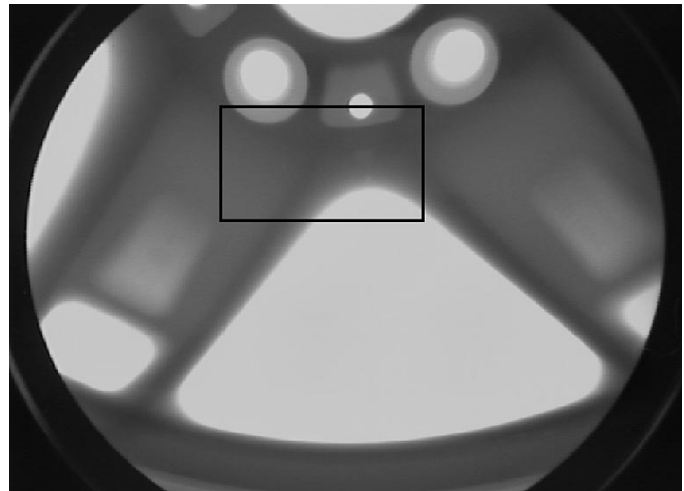


Fig. 1. Radioscopic image of a casting (see zoom in Fig. 2).

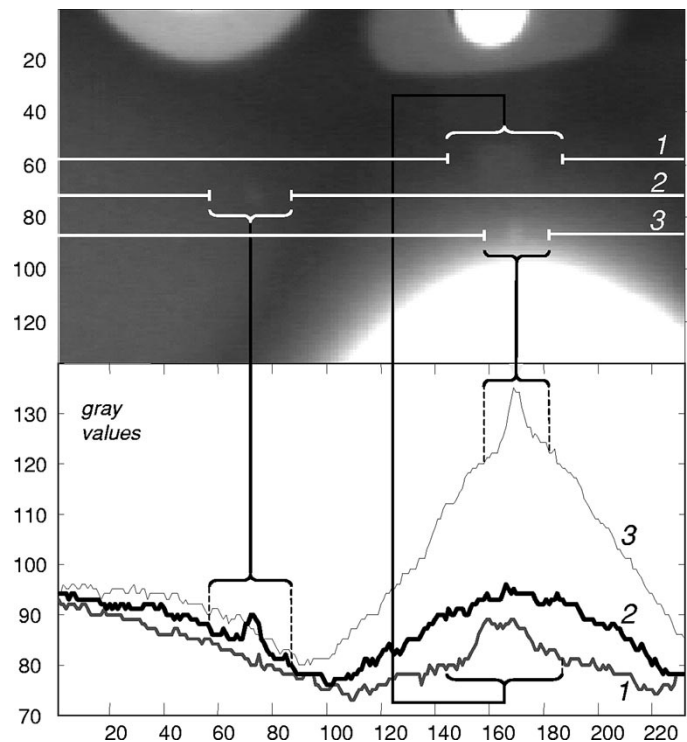


Fig. 2. Zoom of Fig. 1 and gray level profile along three rows crossing defects.

Over the past decade, radioscopic systems have been introduced in the automotive manufacturing industry in order to

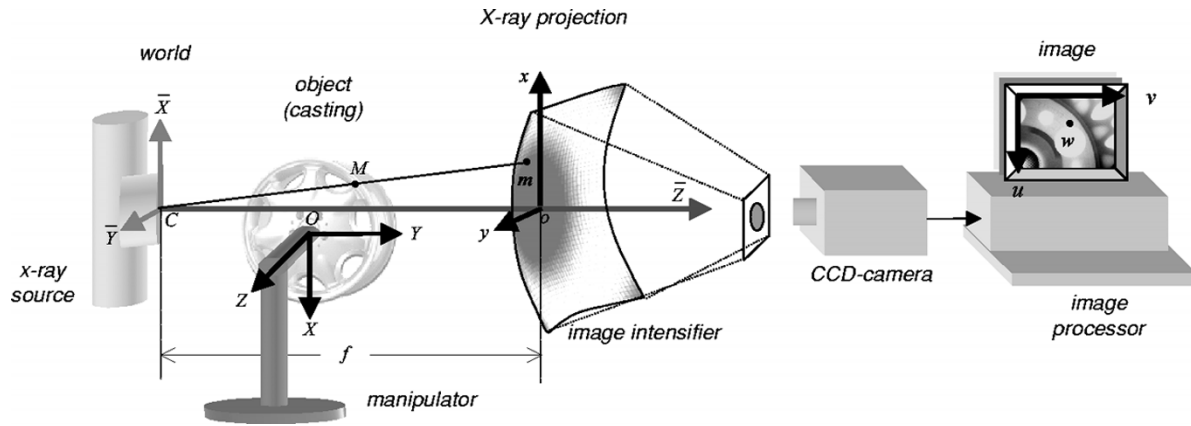


Fig. 3. Automated X-ray inspection system and its coordinate systems. World: $(\bar{X}, \bar{Y}, \bar{Z})$. Object: (X, Y, Z) . X-ray projection: (x, y) . Image: (u, v) .

detect flaws automatically without human interaction [2]–[4]. Over the years, they have not only increased quality through repeated objective inspections and improved processes, but have also increased productivity through decreased labor cost. An automated X-ray system is schematically presented in Fig. 3. The inspection is typically performed in five steps. 1) The *manipulator* places the casting in the desired position. 2) The *X-ray tube* generates X-rays which pass through the casting. 3) The X-rays are detected by the fluorescent entrance screen of the *image intensifier*, amplified, and depicted onto a phosphor screen. The image intensifier converts the X-rays to a visible radioscopic image. 4) The guided and focused image is registered by the *charge-coupled device (CCD) camera*. 5) The *image processor* converts the analog video signal, transferred by the CCD camera, into a digital data stream. Digital image processing is used to improve and evaluate the radioscopic image.

In order to inspect the whole object, radioscopic images at different positions of the casting are taken and processed. The classic image-processing methods for flaw detection [3]–[7] consist of a bank of filters which generate an error-free reference image from the radioscopic image taken. Flaws are detected at pixels where the difference between them is considerable. Using *a priori* knowledge of the regular structures of the castings, each programmed view is subdivided into several segments to enable the use of the best type of filter for each part of the image. Varying the matrix size and the directions of the mask filters, they can be adapted to the regular structures of the specimen. This procedure is repeated at each programmed position of the casting. The disadvantages of these methods are as follows. 1) The filters must be configured and tuned manually for each casting and position. If the casting is not exactly placed at the required position, the filter might not work correctly and the detection may fail. 2) The filter parameters, like size and direction of the filter mask, depend strongly on the size and shape of the structure of the casting. 3) Useful information about the correspondence between the different views of the casting is not taken into account.

A review of the existing approaches of automated flaw detections in aluminum castings can be found in [1]. Other

methods, such as the combined median filter [8], the intelligent knowledge-based technique [9], the feature-based approach [2], and the neural networks procedure [10] attempt to detect flaws without *a priori* information about the location of regular structures. The prerequisite for the use of a method from this group is the existence of common properties which define all casting defects well, and also differentiate them from design features of the test pieces. These prerequisites are often fulfilled only in special testing situations. For this reason, the true positive and false positive rates of these methods seem to be unsatisfactory in order to gain acceptance in industry.

Motivated by visual inspections that are able to differentiate between regular structures and defects by looking at the moving radioscopic image of the casting under test, we present in this paper a new method of automated inspection of aluminum castings using radioscopic image sequences.¹ Our method uses a single filter, independent of the placement and the structure of the specimen, to detect suspected defective regions in each radioscopic image. The number of potential flaws that can be identified is enormous. However, if one tries to match and track them in the image sequence using geometric and algebraic constraints on correspondences in multiple views, it is possible to separate the real defects from the false ones. The key idea of this work is to consider only those that can be tracked in the image sequence as real defects.

The paper is organized as follows. In Section II, the geometric model is introduced. Section III describes our method. The results obtained on radioscopic images, with both real data in which synthetic flaws have been added and real radioscopic image sequences, and a comparison with other methods, are presented in Section IV. Finally, Section V gives concluding remarks and suggestions for future research. An early version of this research is presented in [12]. For an extended version of this paper, see [13].

¹A similar idea is also used by radiologists that analyze two different view X-rays of the same breast to detect cancer in its early stages. Thus, the number of cancers flagged erroneously and missed cancers may be greatly reduced (see, for example, [11], where a novel method that automatically finds correspondences in two different views of the breast is presented).

II. GEOMETRIC MODEL OF THE RADIOSCOPIC SYSTEM

In this section, a model is presented which relates the three-dimensional (3-D) coordinates of the casting (*object*), to the 2-D coordinates of the radioscopic image pixel. Additionally, we establish the geometric and algebraic constraints between two and three radioscopic images taken at different positions of the object. Finally, the problem of 3-D reconstruction using a least-squares technique is described.

Since the X-ray images are taken at N different positions of the object, an index p , $p = 1, \dots, N$, is used to denote the position p of the object. It is assumed that the imaging system is calibrated (for details, see Appendix A).

A. Coordinate Systems

One can define the following coordinate systems to describe the relationship between the 3-D object point and the 2-D pixel, as shown in Fig. 3.

The 3-D **object coordinate system** is attached to the object. An object 3-D point M in this coordinate system is denoted by $\mathbf{M} = [X \ Y \ Z \ 1]^T$ in projective coordinates.² The center of rotation of the object is assumed at the origin O of this coordinate system. The motion of the object is considered as a rotation around the origin, followed by a translation. The coordinates of M in the object coordinate system are independent of the object displacement, i.e., $\mathbf{M} = \mathbf{M}_p$.

The 3-D **world coordinate system** is defined in the optical center of the central projection, i.e., its origin C corresponds to the X-ray source. The object point M at position p in this coordinate system is $\bar{\mathbf{M}}_p = [\bar{X}_p \ \bar{Y}_p \ \bar{Z}_p \ 1]^T$ in projective coordinates. The object coordinate system is then considered as a rigid displacement of the world coordinate system represented by a 3×3 rotation matrix \mathbf{R}_p and a 3×1 translation vector \mathbf{t}_p [14]. With the 4×4 matrix \mathbf{S}_p

$$\mathbf{S}_p = \begin{bmatrix} \mathbf{R}_p & \mathbf{t}_p \\ \mathbf{0} & 1 \end{bmatrix} \quad (1)$$

one obtains the relationship between object and world coordinate system

$$\bar{\mathbf{M}}_p = \mathbf{S}_p \mathbf{M}. \quad (2)$$

Now, a 2-D **X-ray projection coordinate system** is defined that indicates the coordinates of a point in the (not visible) X-ray image at a fictitious plane $\bar{Z} = f$ located at the entrance screen of the image intensifier. Its origin o is pierced by the \bar{Z} axis. The X-rays make a linear perspective projection of the point M onto a point m_p (at position p) in the fictitious plane without any distortion. Applying Thales' theorem, the projective coordinates of m_p in this 2-D system are $\mathbf{m}_p = [x_p \ y_p \ 1]^T$, with $x_p = f\bar{X}_p/\bar{Z}_p$ and $y_p = f\bar{Y}_p/\bar{Z}_p$. Using $\bar{\mathbf{M}}_p$ and \mathbf{m}_p as projective

²We use the notation of Faugeras [14], where we differentiate between the projective geometric objects themselves and their representations (e.g., a point in the space will be denoted by M , whereas its vector in projective coordinates will be denoted by \mathbf{M}).

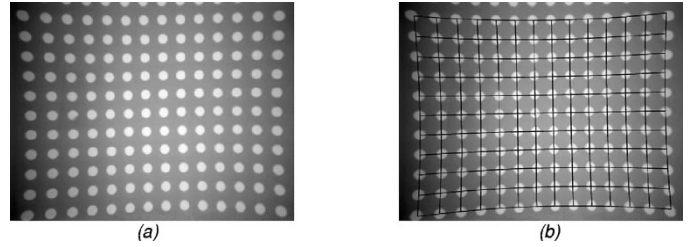


Fig. 4. X-ray of the calibration plate and its modeled grid.

representations of M and m_p , respectively, the following linear equation is obtained:

$$\lambda_p \mathbf{m}_p = \underbrace{\begin{bmatrix} f & 0 & 0 & 0 \\ 0 & f & 0 & 0 \\ 0 & 0 & 1 & 0 \end{bmatrix}}_{\mathbf{B}} \bar{\mathbf{M}}_p \quad (3)$$

where λ_p is a scale factor. One may denote by $\mathbf{P}_p = \mathbf{B}\mathbf{S}_p$ the 3×4 perspective projection matrix at position p . From (2) and (3), one obtains the equation that maps object coordinates to X-ray projection plane coordinates at the position p of the object

$$\lambda_p \mathbf{m}_p = \mathbf{P}_p \mathbf{M}. \quad (4)$$

Finally, the 2-D **image coordinate system** is introduced as a representation of the pixel coordinates of the (visible) radioscopic image formed at the CCD camera. The point \mathbf{m}_p is projected onto the plane of the CCD array as $\mathbf{w}_p = [u_p \ v_p \ 1]^T$ in projective coordinates. Due to the curvature of the entrance screen of the image intensifier and the electromagnetic fields that may be present in the radioscopic system, the radioscopic image received by the CCD camera is deformed, especially at the corners of the image. Therefore, the relationship between X-ray projection and image coordinate system is nonlinear

$$\mathbf{w}_p = \mathbf{f}(\mathbf{m}_p). \quad (5)$$

The nonlinear function \mathbf{f} can be cubic [15] or hyperbolic, as shown in Appendix A. A way to estimate this function is by analyzing the projective distortion of a calibration plate which contains holes placed in a regular grid manner. The phenomenon of the distortion effect is illustrated in the radioscopic image of the calibration plate [Fig. 4(a)]. The modeled hyperbolic grid is shown in Fig. 4(b).

Using (4) and (5), a relation can be made between the 3-D coordinates of the object and the radioscopic image pixel coordinates at each position of the object.

In Sections II-B–D, geometric and algebraic constraints are considered to solve the correspondence problem between radioscopic images at different positions of the object, and the 3-D reconstruction problem taking corresponding points in these images. In the approach, a point \mathbf{w}_p , found in the radioscopic image p , is first transformed into the coordinates of the X-ray projection coordinate system using the inverse transformation of (5): $\mathbf{m}_p = \mathbf{f}^{-1}(\mathbf{w}_p)$. With this nonlinear transformation, one can use the linear relationship (4) explained above.

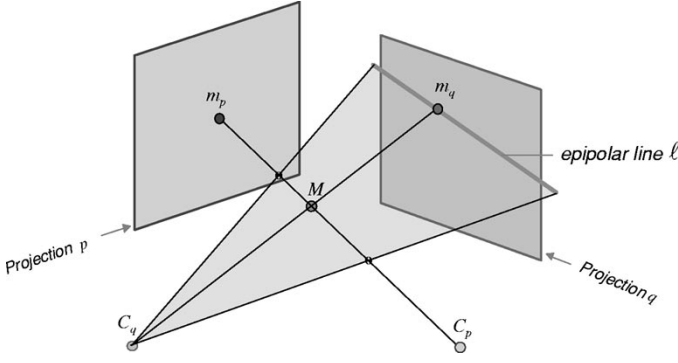


Fig. 5. Epipolar geometry between two views.

B. Correspondence Between Two Views

Now, the correspondence between two points m_p and m_q (in the X-ray projection coordinate system) is considered. The first one is obtained by projecting the object point M at position p , and the second one at position q .

To solve the problem of the correspondence, we use epipolar geometry [14]. The epipolar constraint is well known in stereo vision. For each projection point m_p at the position p of the object, its corresponding projection point m_q at the position q of the object lies on the epipolar line ℓ of m_p , as shown in Fig. 5, where C_p and C_q are the centers of projections p and q , respectively. In this representation, a rotation and translation relative to the object coordinate system is assumed. The epipolar line ℓ can be calculated as the projection of line $\langle m_p, C_p \rangle$ by the center of projection C_q in projection plane q . After some manipulations, one obtains the linear relationship

$$\mathbf{m}_q^T \mathbf{F}_{pq} \mathbf{m}_p = 0 \quad (6)$$

where \mathbf{F}_{pq} is the well-known 3×3 fundamental matrix between projections p and q , which depends only on perspective projection matrices \mathbf{P}_p and \mathbf{P}_q [16].

C. Correspondence Between Three Views

Given three points m_p , m_q , and m_r (at positions p , q and r , respectively), the projection of the corresponding 3-D point M into the three views may be expressed as a single matrix equation using (4) [16]

$$\underbrace{\begin{bmatrix} \mathbf{P}_p & \mathbf{m}_p & 0 & 0 \\ \mathbf{P}_q & 0 & \mathbf{m}_q & 0 \\ \mathbf{P}_r & 0 & 0 & \mathbf{m}_r \end{bmatrix}}_{\mathbf{G}} \underbrace{\begin{bmatrix} \mathbf{M} \\ -\lambda_p \\ -\lambda_q \\ -\lambda_r \end{bmatrix}}_{\mathbf{v}} = \mathbf{0}. \quad (7)$$

If m_p , m_q , and m_r are corresponding points, then there exists a nontrivial solution of \mathbf{v} in (7). It follows that any 7×7 minor of the 9×7 matrix \mathbf{G} has a zero determinant. This condition leads to four independent trilinear relationships (Shashua's trilinearities), between the vectors \mathbf{m}_p , \mathbf{m}_q , and \mathbf{m}_r . Using a structure called the *trifocal tensor*, which depends only on perspective projection matrices \mathbf{P}_p , \mathbf{P}_q , and \mathbf{P}_r , one can

directly compute the coordinates of the third point m_r , given the points m_p and m_q .

D. 3-D Reconstruction From Two or More Views

It is assumed that there are n projections (at n different positions), in which the corresponding points m_i , $i = 1, \dots, n$, with coordinates (x_i, y_i) are presented. To reconstruct the corresponding 3-D point M that may have produced these projection points, (4) is used in each position: $\lambda_i \mathbf{m}_i = \mathbf{P}_i \mathbf{M}$. Each projection yields three linear equations in the unknowns X , Y , Z , and λ_i . After some slight rearranging, one obtains an overdetermined system, which can be solved for $[X \ Y \ Z]^T$ using a least-squares technique [14].

III. AUTOMATED DETECTION OF FLAWS

The method to automated flaw detection presented here has basically two steps: *identification* and *tracking* of potential flaws. They will be described in this section.

A. Identification of Potential Flaws

After the image is acquired by the CCD camera, digital radioscopic images are generated using a frame grabber. In order to ensure the tracking of flaws in the radioscopic images, similar projections of the specimen must be achieved along the sequence. For this reason, the sequence consists of radioscopic images taken by rotation of the casting at small intervals (e.g., 5°). Since many images are captured, the time of the data acquisition is reduced by taking the images without frame averaging. The position of the casting, provided online by the manipulator, is registered at each radioscopic image to calculate the perspective projection matrix \mathbf{P}_p (for details, see Appendix A). A radioscopic sequence is shown in Fig. 6.³

The detection of potential flaws identifies regions in radioscopic images that may correspond to real defects. This process takes place in each radioscopic image of the sequence without considering information about the correspondence between them. Two general characteristics of the defects are used to identify them: 1) a flaw can be considered as a connected subset of the image; and 2) the gray level difference between a flaw and its neighborhood is significant. However, since the signal-to-noise ratio (SNR) in our radioscopic images is low, the flaws signal is slightly greater than the background noise, as illustrated in Fig. 2. In our experiments, the mean gray level of the flaw signal (without background) was between 2.4 and 28.8 gray values with a standard deviation of 6.1. Analyzing a homogeneous background in different areas of interest of normal parts, we obtained that the noise signal was within ± 13 gray values with a standard deviation of 2.5. For this reason, the identification of real defects with poor contrast can involve as well the detection of false alarms.

According to the mentioned characteristics of the real flaws, our method of identification has the following two steps (see Fig. 7).

³The radioscopic sequences shown in this paper are available at <http://www.diinf.usach.cl/~dmery/sequences.htm>.

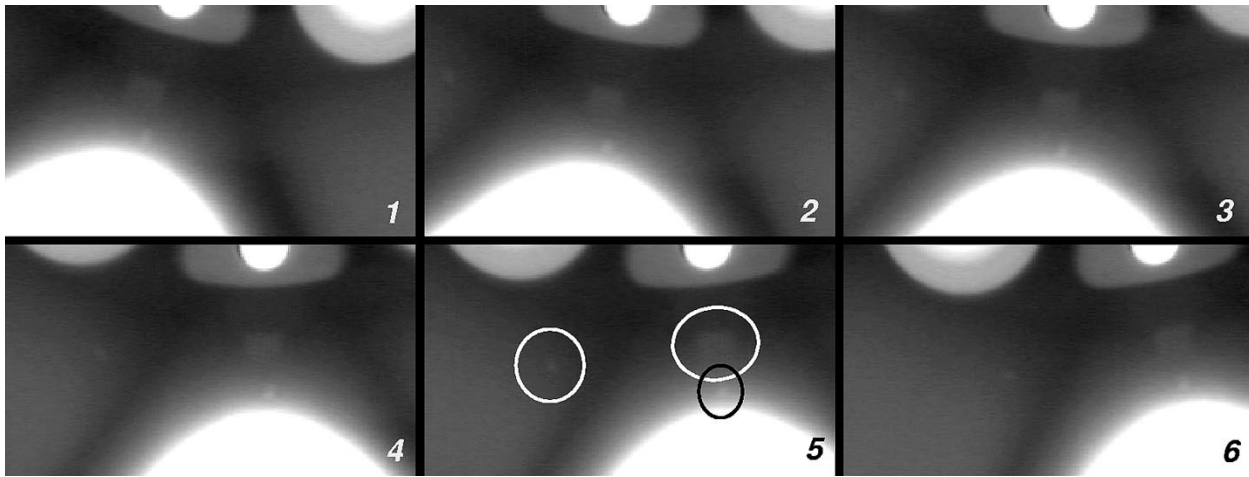


Fig. 6. Radioscopic sequence with three flaws (image 5 is shown in Fig. 2).

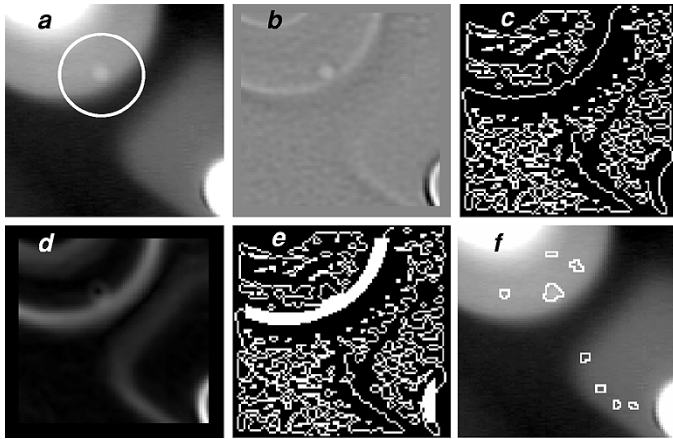


Fig. 7. Identification of potential flaws. (a) Radioscopic image with a small flaw at an edge of a regular structure. (b) Laplacian-filtered image with $\sigma = 1.25$ pixels (kernel size = 11×11). (c) Zero crossing image. (d) Gradient image. (e) Edge detection after adding high gradient pixels. (f) Potential flaws.

Edge detection: A Laplacian-of-Gaussian (LoG) kernel and a zero-crossing algorithm [14] are used to detect the edges of the radioscopic images. The LoG operator involves a Gaussian lowpass filter, which is a good choice for the presmoothing of our noisy images. The resulting binary edge image should produce at real flaws closed and connected contours which demarcate regions. However, a flaw may not be perfectly enclosed if it is located at an edge of a regular structure as shown in Fig. 7(c). In order to complete the remaining edges of these flaws, a thickening of the edges of the regular structure is performed as follows: 1) the gradient image⁴ of the original image is computed [see Fig. 7(d)]; 2) by thresholding the gradient image at a high gray level a new binary image is obtained; and 3) the resulting image is added to the zero-crossing image [see Fig. 7(e)].

⁴The gradient image is computed by taking the square root of the sum of the squares of the gradient in horizontal and in vertical direction. They are calculated by the convolution of the radioscopic image with the first derivative (in the corresponding direction) of the Gaussian lowpass filter used in the LoG filter.

Segmentation and classification of potential flaws: Afterwards, each closed region is segmented and classified as potential flaw if its mean gray level is 2.5% greater than the mean gray level of its surroundings (to ensure the detection of the flaws with poor contrast), and its area is greater than 15 pixels (very small flaws are allowed). A statistical study of the classification of potential flaws using more than 70 features can be found in [17].

This is a very simple detector of potential flaws. However, the advantages are that it is a single detector (it is the same detector for each image), and it is able to identify potential defects independent of the placement and the structure of the specimen. As mentioned in Section I, the classic methods use *a priori* information and their configuration is a very complicated task.

Using this method, some real defects cannot be identified in all radioscopic images in which they appear if the contrast is very poor or the flaw is not enclosed by edges. For example, in Fig. 8 one can observe that the biggest real flaw was identified in images 1, 2, 3, 4 and 6, but not in image 5, where only two of the three real flaws were identified (compare with Fig. 2). Additionally, if a flaw is overlapped by edges of the structure of the casting, not all edges of the flaw can be detected. In this case, the flaw will not be enclosed, and therefore, not be segmented. Furthermore, a small flaw that moves in front (or behind) a thick cross section of the casting, in which the X-rays are highly absorbed, may cause an occlusion. In our experiments, this detector identified the real flaws in four or more (not necessarily consecutive) images of the sequence.

B. Tracking of Potential Flaws

After the potential flaws in each radioscopic image are identified, the attempt is made to track them in the image sequence in order to separate the false detections from the real ones. The tracking consists of three steps: matching in two views, tracking in more views, and verification.

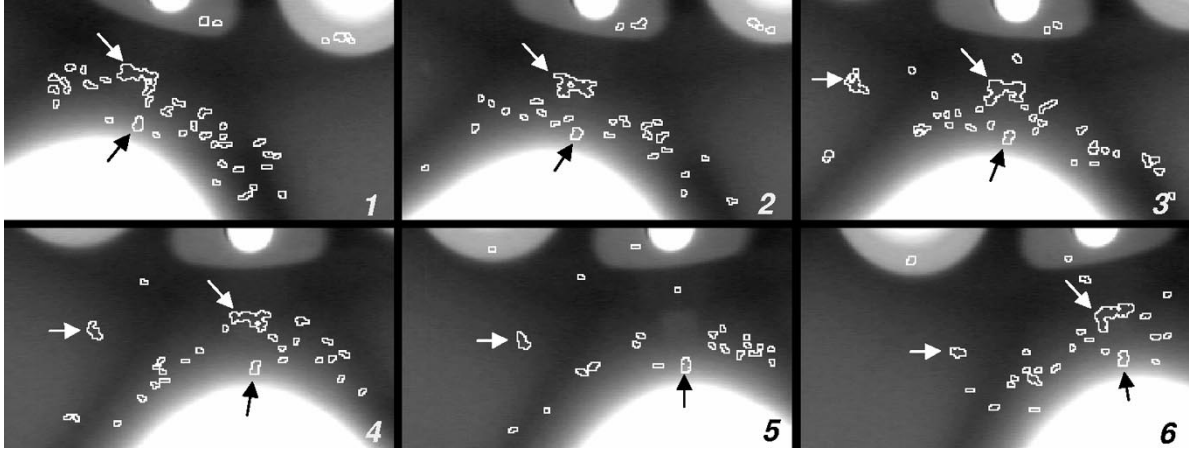


Fig. 8. Identification of potential flaws (the arrows indicate real flaws).

1) *Matching in Two Views*: Matching requires the position and the extracted features of each detected potential flaw. In this work, $\mathbf{a} = (a, p)$ will denote the identified region (potential flaw) a in image p . It is assumed that the image sequence has N images ($1 \leq p \leq N$) and n_p regions were identified in image p ($1 \leq a \leq n_p$). The position and the features of region $\mathbf{a} = (a, p)$ are arranged in a position vector \mathbf{m}_p^a and a feature vector \mathbf{z}_p^a , respectively. The center of gravity is taken as the position of the region. Its coordinates are transformed into the coordinates of the X-ray projection coordinate system using the inverse function \mathbf{f}^{-1} of (5). One obtains then the position vector $\mathbf{m}_p^a = [x_p^a \ y_p^a \ 1]^T$. The feature vector contains the set of n extracted and normalized features of the region, $\mathbf{z}_p^a = [z_p^a(1) \ z_p^a(2) \ \dots \ z_p^a(n)]^T$.

This step matches two regions (of two views), region $\mathbf{a} = (a, p)$ with region $\mathbf{b} = (b, q)$, for $p \neq q$, if they fulfill all following matching conditions.

Epipolar constraint: the centers of gravity of the regions must satisfy the epipolar constraint. To investigate if \mathbf{m}_p^a and \mathbf{m}_q^b satisfy the epipolar constraint, the criterion is chosen, whereby the perpendicular Euclidean distance from the epipolar line of the point \mathbf{m}_p^a to the point \mathbf{m}_q^b must be smaller than ε_2 [16]

$$\frac{|\mathbf{m}_q^{bT} \mathbf{F}_{pq} \mathbf{m}_p^a|}{\sqrt{\ell_x^2 + \ell_y^2}} < \varepsilon_2 \quad (8)$$

where $[\ell_x \ \ell_y \ \ell_z]^T = \mathbf{F}_{pq} \mathbf{m}_p^a$ and \mathbf{F}_{pq} is the fundamental matrix (see Section II-B).

Similarity condition: the regions must be similar enough. To evaluate this criterion, a degree of similarity S is calculated as the Euclidean distance between the normalized feature vectors of the regions. The degree of similarity of the regions must be smaller than ε_s , i.e., $S(\mathbf{z}_p^a, \mathbf{z}_q^b) = \|\mathbf{z}_p^a - \mathbf{z}_q^b\| < \varepsilon_s$.

Correct location in 3-D: the 3-D point reconstructed from the centers of gravity of the regions must belong to the space occupied by the casting. From \mathbf{m}_p^a and \mathbf{m}_q^b , the corresponding 3-D point $\hat{\mathbf{M}}$ is estimated using the linear approach of Hartley [16]. For two views, this approach is faster than the least-squares technique. It is necessary to examine whether $\hat{\mathbf{M}}$ resides in

the volume of the casting, the dimensions of which are usually known *a priori* (e.g., a wheel is assumed to be a cylinder).⁵

The matching conditions in both identified regions $\mathbf{a} = (a, p)$ and $\mathbf{b} = (b, q)$ are evaluated in three consecutive frames, for $p = 1, \dots, N-3$, $q = p+1, \dots, p+3$, $a = 1, \dots, n_p$, and $b = 1, \dots, n_q$. If a potential flaw is not matched with any other one, it will be considered as false. Multiple matching, i.e., a region that is matched with more than one region, is allowed. Using this method, the mentioned identification problems (nonclassified or occluded flaws), can be solved by the tracking if a flaw is not identified in consecutive views. Applying this method, the real flaws are successfully matched and a great number of false detections are eliminated. However, the number of the remaining false detections must still be reduced. The results of our example are shown in Fig. 9.

2) *Tracking in More Views*: A match between two regions \mathbf{a} and \mathbf{b} will be denoted by $\mathbf{a} \leftrightarrow \mathbf{b}$ or $(a, p) \leftrightarrow (b, q)$. A $m_2 \times 4$ matrix $\mathbf{A} = [\mathbf{a}_{i1} \ \mathbf{a}_{i2}] = [(a_i, p_i) \ (b_i, q_i)]$, $i = 1, \dots, m_2$, is defined, where m_2 is the number of all matches determined in Section III-B.1.

In the tracking problem, it is required to find trajectories of regions in different views. To establish the correspondence of regions in three images, one seeks all possible links of three regions in matrix \mathbf{A} that satisfy the condition of correspondence between three views. The procedure is as follows. One looks for all two rows i and j of \mathbf{A} ($i, j = 1, \dots, m_2$ and $i \neq j$) that satisfy

$$\mathbf{a}_{i2} = \mathbf{a}_{j1}. \quad (9)$$

Supposing that $i = I$ and $j = J$ fulfill this condition, e.g., $\mathbf{A}_I = [(a, p) \ (b, q)]$ and $\mathbf{A}_J = [(b, q) \ (c, r)]$, one finds three regions $(a, p) \leftrightarrow (b, q) \leftrightarrow (c, r)$ with coordinates \mathbf{m}_p^a , \mathbf{m}_q^b , and \mathbf{m}_r^c , respectively, that could be corresponding regions. To examine if they really correspond to each other, $\hat{\mathbf{m}}_r^c$ is calculated, i.e., the estimation of the coordinates of the third region \mathbf{m}_r^c , from the coordinates of the first two regions \mathbf{m}_p^a and \mathbf{m}_q^b using the

⁵It is possible to use a CAD model of the casting to evaluate this criterion in a more precise way. With this model, we could discriminate a small hole of the regular structure that is identified as potential flaw. Additionally, the CAD model can be used to inspect the casting geometry, as shown in [18].

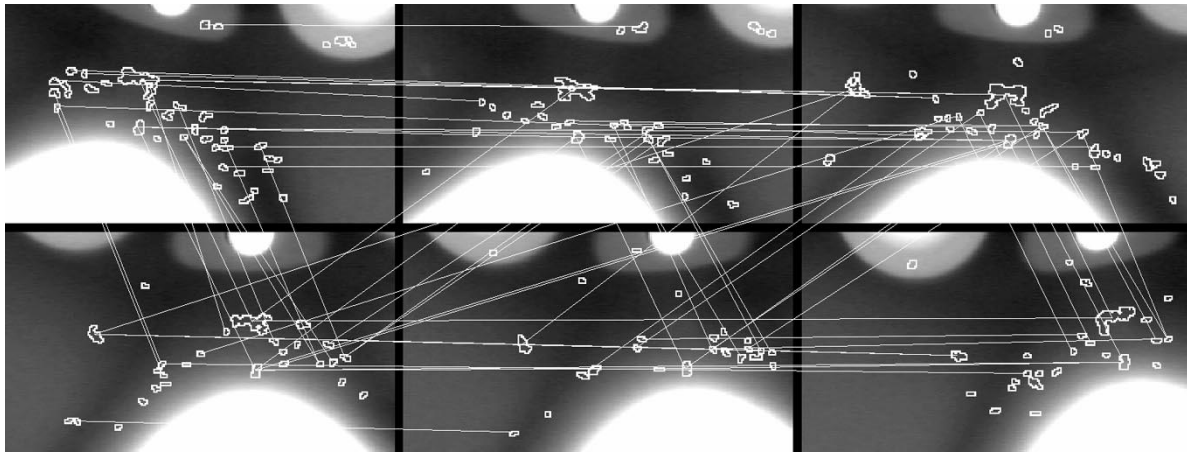


Fig. 9. Matching of potential flaws in two views.

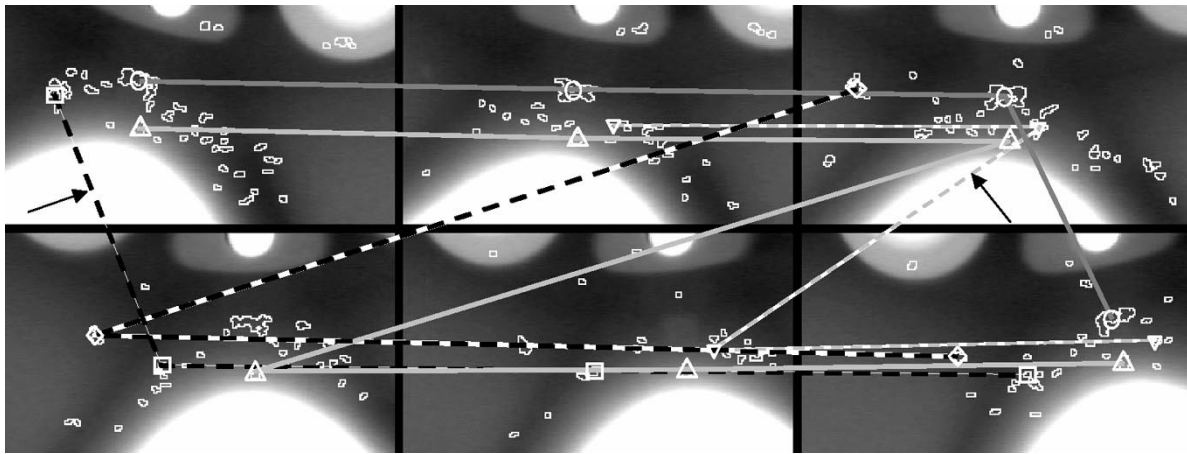


Fig. 10. Tracking in more views (the arrows indicate false detections).

trilinearities of Shashua mentioned in Section II-C. It is assumed that the regions are corresponding, if $\|\hat{\mathbf{m}}_r^c - \mathbf{m}_r^c\| < \varepsilon_3$. The nontracked regions are eliminated, while the m_3 linked triplets are arranged in a new $m_3 \times 6$ matrix $\mathbf{B} = [\mathbf{b}_{i1} \ \mathbf{b}_{i2} \ \mathbf{b}_{i3}]$, $i = 1, \dots, m_3$.

This procedure is repeated to determine trajectories of regions in four radioscopic images. Given four points (in four views), if the first three are corresponding points and the last three are corresponding points too, then all of them are corresponding points, i.e., to seek quadruplets that satisfy the condition of correspondence in four views, it is necessary to look for all rows i and j of \mathbf{B} for $(i, j = 1, \dots, m_3 \text{ and } i \neq j)$ that satisfy

$$\mathbf{b}_{i2} = \mathbf{b}_{j1} \text{ and } \mathbf{b}_{i3} = \mathbf{b}_{j2}. \quad (10)$$

Given the rows $i = I$ and $j = J$ that fulfill this condition, e.g., $\mathbf{B}_I = [(a, p) \ (b, q) \ (c, r)]$ and $\mathbf{B}_J = [(b, q) \ (c, r) \ (d, s)]$, four corresponding regions $(a, p) \leftrightarrow (b, q) \leftrightarrow (c, r) \leftrightarrow (d, s)$ (with coordinates \mathbf{m}_p^a , \mathbf{m}_q^b , \mathbf{m}_r^c , and \mathbf{m}_s^d , respectively) are found. The m_4 detected quadruplets are placed in a new $m_4 \times 8$ matrix $\mathbf{C} = [\mathbf{c}_{i1} \ \mathbf{c}_{i2} \ \mathbf{c}_{i3} \ \mathbf{c}_{i4}]$, $i = 1, \dots, m_4$. Fig. 10 shows the tracked regions of our example that fulfill this criterion. Only two false trajectories are observed (see arrows).

Since our detector cannot guarantee the identification of all real flaws in more than four views, a tracking in five views could lead to the elimination of those real flaws that were identified in only four views. However, if a potential flaw is identified in more than four views, more than one quadruplet can be detected. For this reason, these corresponding quadruplets are joined in a trajectory that contains more than four potential flaws (see trajectory with \triangle in Fig. 10).

3) *Verification*: Using the least-squares technique mentioned in Section II-D, one can estimate the corresponding 3-D point $\hat{\mathbf{M}}$ from the centers of gravity of the tracked regions that may produce each determined trajectory. This 3-D point can be projected in the views where the identification of the tracked flaw has failed to obtain the complete tracking in the radioscopic sequence. The projected points of $\hat{\mathbf{M}}$ should correspond to the centers of gravity of the projected flaws. Now, one can calculate the size of the projected flaw as an average of the sizes of the identified flaws in the trajectory. In each view, a small window is defined with the estimated size in the computed centers of gravity (see Fig. 11). Afterwards, the corresponding windows are averaged. Thus, the attempt is made to increase the SNR by the factor \sqrt{n} , where n is the number of averaged windows. Since flaws must appear as contrasted zones relating to their environment, we verify whether the contrast of each

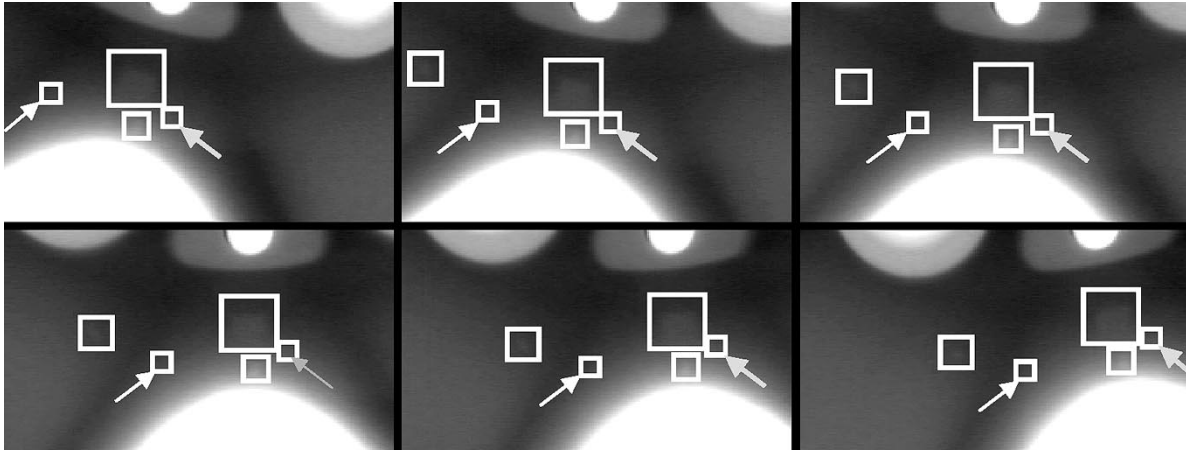


Fig. 11. Reconstruction and verification. The false detections (indicated by the arrows) are eliminated after the verification.

averaged window is greater than 2.5%. With this verification, it is possible to eliminate all remaining false detections. Fig. 11 shows the detection in our sequence using this method. Our objective is then achieved: the real defects were separated from the false ones.

IV. EXPERIMENTAL RESULTS

In this section, results of automatic inspection of cast aluminum wheels using the approach outlined in Section III are presented. These results have been achieved recently on synthetic flaws and real data. The parameters of our method have been manually tuned, giving $\sigma = 1.25$ pixels (for LoG-operator), $\varepsilon_2 = 0.75$ mm, $\varepsilon_s = 0.7$, and $\varepsilon_3 = 0.9$ mm. These parameters were not changed during these experiments. A wheel was considered to be a cylinder with the following dimensions: 470-mm diameter and 200-mm height. The optical focal length (distance between X-ray source and entrance screen of the image intensifier) was 884 mm. The bottom of a wheel was 510 mm from the X-ray source. Thus, a pattern of 1 mm in the middle of the wheel is projected in the X-ray projection coordinate system as a pattern of 1.73 mm, and in the image coordinate system as a pattern of 2.96 pixels. The sequences of radioscopic images were taken by rotation of the casting at 5° .

The detection performance will be evaluated by computing the number of true positives (TP) and false positives (FP). They are, respectively, defined as the number of flaws that are correctly classified and the number of misclassified regular structures. The TP and FP will be normalized by the number of existing flaws (E) and the number of identified potential flaws (I). Thus, we define the following percentages: $TPP = TP/E \times 100$ and $FPP = FP/I \times 100$. Ideally, $TPP = 100\%$ and $FPP = 0\%$.

A. Synthetic Flaws

To evaluate the performance of our method in critical cases, real data in which synthetic flaws have been added were examined. A simple 3-D modeled flaw (a spherical bubble) was projected and superimposed on real radioscopic images of an

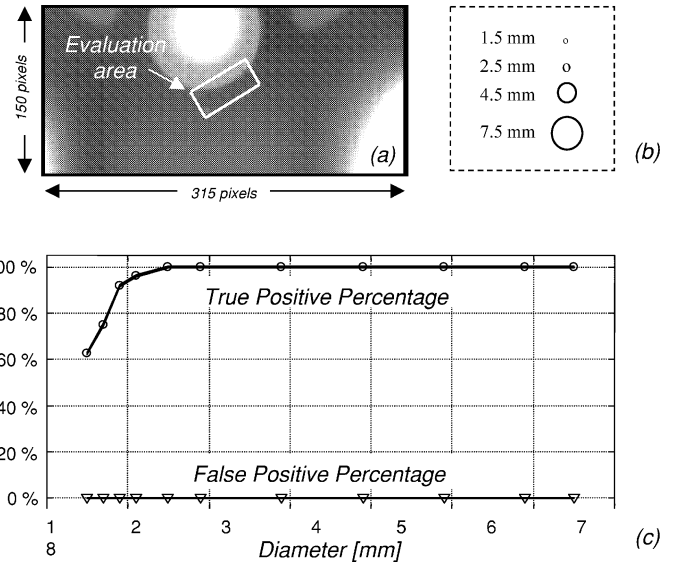


Fig. 12. Detection on synthetic flaws. (a) Radioscopic image and evaluated area. (b) Flaw sizes. (c) TPP and FPP.

aluminum wheel according to the law of X-ray absorption [19]. In our experiment, a flaw is simulated in ten radioscopic images of a real casting, in an area that included an edge of the structure [see Fig. 12(a)]. In this area, the synthetic flaw was located in 24 different positions in a regular grid manner. At each position, TPP and FPP were tabulated. This test was repeated for different sizes of the flaws ($\phi = 1.5$ –7.5 mm) which are illustrated in Fig. 12(b). The results are shown in Fig. 12(c). It was observed that the FPP was always zero. The TPP was 100% for $\phi \geq 2.5$ mm, and greater than 95% for $\phi \geq 2.1$ mm. However, the identification of the flaw may fail (and therefore, also its detection) if it is very small and is located at the edge of the structure of the casting. In this case, one may choose a smaller value of the parameter σ in the LoG operator of the edge detection, which will unfortunately increment the FPP. Other noncritical experiments, where the area of the simulation does not include an edge of the structure, have led to perfect results ($TPP = 100\%$, $FPP = 0\%$) for $\phi \geq 1.5$ mm (≥ 4.4 pixels).

TABLE I
DETECTION OF FLAWS ON REAL DATA

Seq.	X-ray images	Flaws in the sequence	Flaws in the images (E)	Identification			Detection	
				TP	FP	Total (I)	TP	FP
1	10	2	12	12	249	261	2	0
2	9	1	9	8	238	246	1	0
3	9	3	23	19	253	272	3	0
4	8	1	8	4	413	417	1	0
5	6	1	6	6	554	560	1	0
6	8	1	8	8	196	204	1	0
7	6	3	18	14	445	459	3	0
8	6	0	0	0	178	178	0	0
9	9	0	0	0	256	256	0	0
10	8	0	0	0	150	150	0	0
11	8	0	0	0	345	345	0	0
12	6	0	0	0	355	355	0	0
13	6	0	0	0	365	365	0	0
14	9	0	0	0	313	313	0	0
Total	108	12	84	71	4310	4381	12	0
Percentage				85%	98%		100%	0%

Usually, the minimum detectable defect size according to inspection specifications is in the order of $\emptyset = 2$ mm. In X-ray testing, smaller flaws can be detected by decreasing the distance of the object test to the X-ray source.

B. Real Data

Fourteen radioscopic image sequences of aluminum wheels with 12 known flaws were inspected. Three of these defects were existing blow holes (with $\emptyset = 2.0$ – 7.5 mm). They were initially detected by a visual (human) inspection. The remaining nine flaws were produced by drilling small holes ($\emptyset = 2.0$ – 4.0 mm) in positions of the casting which were known to be difficult to detect. Casting flaws are present only in the first seven sequences. The results are summarized in Table I, Fig. 13, and Fig. 14. In the identification of potential flaws, it was observed that the FPP was 98% (4310/4381). Nevertheless, the TPP in this experiment was good, it was possible to identify 85% (71/84) of all projected flaws in the sequences (13 of the existing 84 flaws were not identified because the contrast was poor or they were located at edges of regular structures). It was observed that in the next steps, the FPP was reduced to nil. The detection of the real flaws was successful in all cases. The first six images of sequence three and its results were already illustrated in Fig. 6, and Figs. 8–11. The results on the other sequences with flaws are shown in Fig. 13.

C. Comparison With Other Methods

In this section, we present a comparison of our proposed algorithm with other methods that can be used to detect defects in aluminum castings. In this comparison, we evaluate the same real 14 sequences used in the previous section. The results are summarized in Table II.

First, we compared the first step of our method (identification of potential flaws). The objective of this step is the use of a single filter, instead of a set of filters adapted to the regular structure of the specimen. We evaluated the well-known Canny filter (see, for example, [14]). Since this filter detects sparse edge pixels that not necessarily produce closed and connected contours at real flaws, the TPP of this detector was unacceptable, only 4% of the real flaws were identified (“Canny I” in Table II). In order to increase the number of closed regions, a dilation of the edges

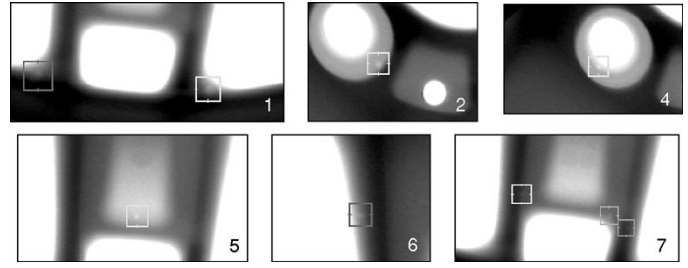


Fig. 13. Detected flaws in sequences 1, 2, 4, 5, 6, and 7 (sequence 3 is shown in Fig. 11).

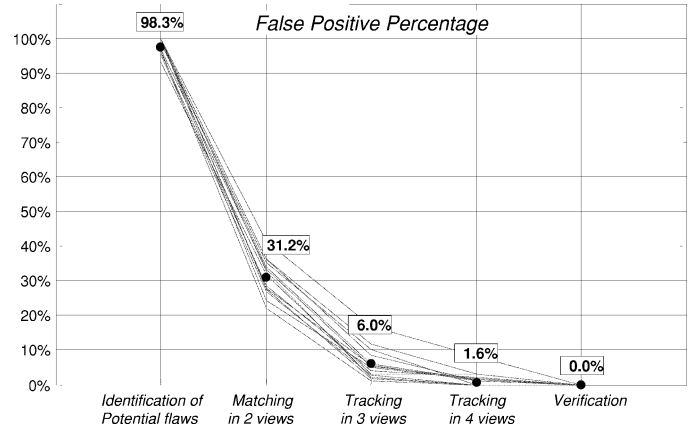


Fig. 14. FP percentage on real data in the 14 real sequences (the number of identified potential flaws corresponds to 100%). The mean of each step (●) is given over the 14 curves.

TABLE II
COMPARISON WITH OTHER METHODS

Method	Identification		Detection	
	TPP	FPP	TPP	FPP
Proposed	85%	98%	100%	0%
Canny I	4%	97%	0%	–
Canny II	40%	99%	17%	40%
Median I	55%	85%	33%	36%
Median II	88%	98%	92%	45%
Tracking in 3	85%	98%	100%	25%
Tracking in 5	85%	98%	83%	0%
PXV-5000	–	–	100%	0%

using a 3×3 mask was performed. Although the TPP is improved to 40% (“Canny II” in Table II), many flaws were not detected in any of the images of the sequence. For this reason, only 17% of the real flaws were detected after the tracking and verification.

Another detection of potential flaws can be performed using a region-based segmentation. Median filtering is normally used to generate an error-free image, since defect structures are essentially eliminated, while design features of the test piece are normally preserved [1]. Once the error-free reference image is computed, an error difference image between original and error-free images is calculated. Casting defects are then detected when a sufficiently large gray level in the error difference image occurs. The best results were obtained using a median filter with a 11×11 mask. We evaluated two thresholds:

$\theta = 6$ and $\theta = 2$ by 256 gray levels (see “Median I” and “Median II” in Table II). In the first case, the TPP was only 55%. By decreasing the threshold value, we increased the TPP to 88%, that is slightly better than our detector (85%). However, systematic false alarms were detected at the corners of the regular structures. Since these false alarms satisfy the multifocal conditions, they can be tracked in the sequence. For this reason, this detector can only be used if the median filter is adapted to the regular structures of the specimen using *a priori* information. Normally, a set of median filters is used for each radioscopic image [3], [4], [6].

In order to evaluate the second step of our method (tracking of potential flaws), we tested the method by tracking the potential flaws in three and in five views, instead of four views (see “Tracking in 3,” “Tracking in 5,” and “Proposed” in Table II). By considering only three views, we obtained so many false alarms that the verification step detected four false alarms (25%). In the other case, by tracking the potential flaws in five views, real flaws that were segmented in only four views of the sequences were not tracked. For this reason, only 83% of the real flaws were detected.

Finally, we inspected the test castings using a classic image-processing method (see explanation in Section I). In our experiments, we used the industrial software PXV-5000 [5], [7]. The results were excellent: 100% of the real flaws were detected without false alarms. As a result of its peak detection performance, the classic image-processing methods have become most widely established in industrial applications. However, these methods suffer from the complicated configuration of the filtering, which is tailored to the test piece. In our experiments, the configuration process has taken two weeks. On the contrary, since our method requires only a few number of parameters, the configuration could be done in hours.

V. SUMMARY

A new method for automated flaw detection in aluminum castings using multiple view geometry has been developed. Our method is very efficient because it is based on a two-step analysis: identification and tracking. The idea was to try to imitate the way a human inspector inspects radioscopic images. First relevant details (potential defects) are detected, followed by tracking them in the radioscopic image sequence. In this way, the false detections can be eliminated without discriminating the real flaws.

The great advantage of our first step is the use of a single filter to identify potential defects, which is independent of the structure of the specimen. Nevertheless, its disadvantages are the false positive percentage is enormous, the true positive percentage could be poor if the flaws to be detected are very small and located at the edge of a structure, and the identification of regions is time consuming. Contrarily, the second step is highly efficient in both discrimination of false detections and tracking of real defects, and is not time consuming, due to the use of the multiple-view tensors.

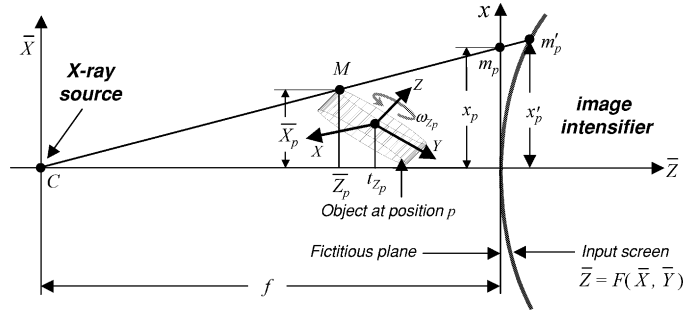


Fig. 15. X-ray projective projection (\bar{Y} and y axes are not shown).

The implementation of our method in industry is nearing completion. The components have been tested in a laboratory prototype. The method was programmed in Visual C++ under Windows NT on a Pentium III system/600 MHz using an image-processing library developed by Intel that includes MMX-instructions [20]. To inspect a whole wheel, our method requires approximately 100 views of 256×256 pixels, that can be processed in one minute. The required computing time is acceptable for practical applications, because a typical inspection process takes about one minute, independent of whether it is performed manually or automatically.

We have shown that these preliminary results are promising. However, since the performance of the method has been verified on a few radioscopic image sequences, an evaluation on a broader data base is necessary.

It is possible to combine our second step with existing defect-detection technologies, which use *a priori* information of the regular structures of the casting to detect flaws in single images (see, for example, [7]). This method could also be used in the automated flaw detection of other objects. In the adaptation of our method, one must determine the number of views in which a flaw must be tracked. If the false positive percentage by identifying potential flaws is small (or high), one may track a flaw in fewer (or more) views of the sequence. However, one must guarantee that the real flaws will be identified as potential flaws in these views.

APPENDIX

CALIBRATION

Equation (4) maps the object coordinates of M to the X-ray projection plane coordinates of m_p at the position p of the object (see Fig. 15). The perspective projection matrix \mathbf{P}_p depends on seven parameters, namely the focal length f , the translation 3-vector $\mathbf{t}_p = [t_{X_p} \ t_{Y_p} \ t_{Z_p}]^T$, and the Euler angles ω_{X_p} , ω_{Y_p} , and ω_{Z_p} between object and world coordinate systems. The Euler angles are used to calculate the 3×3 rotation matrix \mathbf{R}_p (see, for example, [16]). In our experiments, the parameters t_{X_p} , t_{Y_p} , t_{Z_p} , ω_{X_p} , and ω_{Y_p} were constant. The different positions of the casting were obtained by rotating the Z axis. This rotation, denoted by ω_{Z_p} , was provided by the manipulator.

Now, we introduce the model that is used to transform the 2-D point $\mathbf{m}_p = [x_p \ y_p \ 1]^T$ (in X-ray projection coordinate system) into the 2-D point $\mathbf{w}_p = [u_p \ v_p \ 1]^T$ (in CCD image coordinate system). The input screen of the image intensifier corresponds normally to a hyperbolic 3-D surface [21], which is defined by

$$\bar{Z} = F(\bar{X}, \bar{Y}) = f \sqrt{1 + \left(\frac{\bar{X}}{a}\right)^2 + \left(\frac{\bar{Y}}{b}\right)^2} \quad (11)$$

with f being the real half axis of the hyperboloid, and a and b the imaginary half axes. We observe that f coincides with the focal length of the X-ray projection. The projection of point M onto the input screen of the image intensifier is denoted by m'_p . It is calculated as the intersection of the line that contains points C , M , and m_p with the 3-D surface F (see Fig. 15). Its coordinates are given by

$$\mathbf{m}'_p = \mathbf{g}(\mathbf{m}_p) = [cx_p \ cy_p \ 1]^T \quad (12)$$

with $c = 1/\sqrt{1 - (x_p/a)^2 - (y_p/b)^2}$. The point m'_p is imaged at the CCD camera as w_p which coordinates can be estimated approximately using an affin transformation

$$\mathbf{w}_p = \begin{bmatrix} +k_x \cos(\theta) & +k_y \sin(\theta) & u_0 \\ -k_x \sin(\theta) & +k_y \cos(\theta) & v_0 \\ 0 & 0 & 1 \end{bmatrix} \mathbf{m}'_p \quad (13)$$

where k_x and k_y are scale factors, and (u_0, v_0) and θ are, respectively, the translation and the rotation between x, y and u, v axes. Denoting by \mathbf{A} the 3×3 matrix of (13), the transformation from \mathbf{m}_p to \mathbf{w}_p is computed as

$$\mathbf{w}_p = \mathbf{f}(\mathbf{m}_p) = \mathbf{A}\mathbf{g}(\mathbf{m}_p). \quad (14)$$

The inverse transformation of \mathbf{f} is given by

$$\mathbf{m}_p = \mathbf{f}^{-1}(\mathbf{w}_p) = \mathbf{g}^{-1}(\mathbf{A}^{-1}\mathbf{w}_p) = [dx'_p \ dy'_p \ 1]^T \quad (15)$$

with $d = 1/\sqrt{1 + (x'_p/a)^2 + (y'_p/b)^2}$.

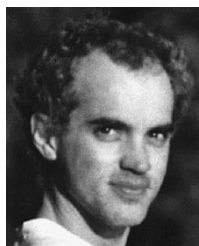
The problem of calibration is to estimate the parameters of our model ($t_X, t_Y, t_Z, \omega_X, \omega_Y, f, a, b, k_x, k_y, \theta, u_0$, and v_0). For this reason, N radiosopic images of a calibration object, with n points whose object coordinates (X_i, Y_i, Z_i) (for $i = 1, \dots, n$) are known, are taken at different positions by rotating the Z axis in $\omega_{Z_1}, \dots, \omega_{Z_p}, \dots, \omega_{Z_N}$. The corresponding image coordinates (u_{ip}, v_{ip}) are measured. Using the projection model (4) and (14), the inferred image projections $(\hat{u}_{ip}, \hat{v}_{ip})$ are calculated from the calibration points (X_i, Y_i, Z_i) . The parameters of the model are estimated by minimizing an objective function defined as the mean Euclidean distance between (u_{ip}, v_{ip}) and $(\hat{u}_{ip}, \hat{v}_{ip})$ [14]. The objective function must be iteratively minimized, starting with an initial value for the parameters. In our experiments, we calibrated the imaging system with $N = 5$ and $n = 18$. The obtained mean error between measured and estimated calibration points was 1.34 pixels.

ACKNOWLEDGMENT

The authors would like to thank the anonymous reviewers for their helpful comments.

REFERENCES

- [1] D. Mery, D. Filbert, and T. Jaeger, "Image processing for fault detection in aluminum castings," in *Analytical Characterization of Aluminum and Its Alloys*, D. S. MacKenzie and G. Totten, Eds. New York: Marcel Dekker, 2002.
- [2] H. Boerner and H. Strecker, "Automated X-ray inspection of aluminum casting," *IEEE Trans. Pattern Anal. Machine Intell.*, vol. 10, pp. 79–91, Jan. 1988.
- [3] D. Filbert, R. Klatte, W. Heinrich, and M. Purschke, "Computer aided inspection of castings," in *Proc. IEEE-IAS Annu. Meeting*, Atlanta, GA, 1987, pp. 1087–1095.
- [4] W. Heinrich, "Automatische Röntgenserienprüfung von Gußteilen," Ph.D. dissertation, Inst. für Allgemeine Elektrotechnik, Technische Univ., Berlin, Germany, 1988.
- [5] J.-M. Kusanetzky and H. Putzbach, "Modern X-ray inspection in the automotive industry," in *Proc. 14th World Conf. NDT*, New Delhi, India, Dec. 8–13, 1996.
- [6] H. Hecker, "Ein Neues Verfahren Zur Robusten Röntgenbildauswertung in Der Automatischen Gußteilprüfung," Ph.D. dissertation, Vom Fachbereich Elektrotechnik Technische Univ., Berlin, Germany, 1995.
- [7] D. Mery, D. Filbert, and N. Parspour, "Improvement in automated aluminum casting inspection by finding correspondence of potential flaws in multiple radiosopic images," in *Proc. 15th World Conf. NDT*, Rome, Italy, Oct. 15–21, 2000.
- [8] T. Wenzel and R. Hanke, "Fast image processing on die castings," in *Proc. Anglo-German Conf. NDT Imaging and Signal Processing*, Oxford, U.K., March 27–28, 1998.
- [9] A. Kehoe and G. A. Parker, "An intelligent knowledge-based approach for the automated radiographic inspection of castings," *NDT & E Int.*, vol. 25, no. 1, pp. 23–36, 1992.
- [10] S. W. Lawson and G. A. Parker, "Intelligent segmentation of industrial radiographic images using neural networks," *Proc. of SPIE, Mach. Vision Applicat. Syst. Integration III*, vol. 2347, pp. 245–255, Nov. 1994.
- [11] Y. Kita, R. Highnam, and M. Brady, "Correspondence between different view breast X-rays using curved epipolar lines," *Comput., Vision, Understanding*, vol. 83, no. 1, pp. 38–56, 2001.
- [12] D. Mery and D. Filbert, "Verfolgung von Gußfehlern in einer digitalen röntgenbildsequenz—eine neue Methode zur Automatisierung der Qualitätskontrolle von Gußteilen," *tm—Technisches Messen*, vol. 67, no. 4, pp. 160–165, 2000.
- [13] D. Mery, "Automatische Gußfehlererkennung aus digitalen Röntgenbildsequenzen," Ph.D. dissertation, Inst. für Meß- und Automatisierungstechnik, Technische Univ., Berlin, Germany, 2000.
- [14] O. Faugeras, *Three-Dimensional Computer Vision: A Geometric Viewpoint*. Cambridge, MA: MIT Press, 1993.
- [15] C. Brack, H. Götte, F. Gossé, J. Moctezuma, M. Roth, and A. Schweikard, "Toward accurate X-ray-camera calibration in computer-assisted robotic surgery," in *Proc. Int. Symp. Computer Assisted Radiology (CAR)*, Paris, France, 1996, pp. 721–728.
- [16] R. I. Hartley and A. Zisserman, *Multiple View Geometry in Computer Vision*. Cambridge, U.K.: Cambridge Univ. Press, 2000.
- [17] D. Mery and D. Filbert, "Classification of potential defects in automated inspection of aluminum castings using statistical pattern recognition," in *Proc. 8th Euro. Conf. Non-Destructive Testing (ECNDT 2002)*, Barcelona, Spain, June 17–21, 2002.
- [18] A. Noble, R. Gupta, J. Mundy, A. Schmitz, and R. Hartley, "High precision X-ray stereo for automated 3-D CAD-based inspection," *IEEE Trans. Robot. Automat.*, vol. 14, pp. 292–302, Apr. 1998.
- [19] D. Mery, "Flaw simulation in castings inspection by radioscopy," *INSIGHT, J. British Inst. Non-Destructive Testing*, vol. 43, no. 10, pp. 664–668, 2001.
- [20] I. Weiske, D. Mery, C. Geisert, and D. Filbert, "Implementation of a method for flaw detection in aluminum castings," *Electron. J. Non-Destructive Testing*, vol. 7, no. 3, Mar. 2002.
- [21] R. Felix and B. Ramm, *Das Röntgenbild*, 3 ed. Stuttgart, Germany: Georg Thieme Verlag, 1988.



Domingo Mery (M'01) received the B.S. degree from the Universidad Nacional de Ingeniería, Perú, in 1989; the Diploma (M.S.) degree in electrical engineering from the Technical University of Karlsruhe, Karlsruhe, Germany, in 1992, and the Ph.D. degree with distinction from the Technical University of Berlin, Berlin, Germany, in 2000.

From 1993 to 1996, he was a Research Assistant at the Department of Electrical Engineering at the Catholic University of Chile. From 1996 to 2000, he was a Research Scientist at the Institute for Measure-

ment and Automation Technology at the Technical University of Berlin with the collaboration of Philips and YXLON X-Ray International. Since 2001, he has been an Assistant Professor at the Departamento de Ingeniería Informática, Universidad de Santiago de Chile. His research interests include image processing for automated inspection, X-ray imaging, nondestructive testing, and computer vision.

Dr. Mery received a scholarship from the Konrad-Adenauer Foundation, and also from the German Academic Exchange Service (DAAD).



Dieter Filbert received the Ph.D. degree in electrical engineering from the Technical University of Berlin, Berlin, Germany in 1970.

Since 1973 he has been a Professor for Measurement Science at the Technical University of Berlin. His main interests are technical diagnosis, model-based measurements, digital test systems, and automated inspection using X-ray testing.